

# In Situ Construction of Manganese Oxide Photothermocatalysts for the Deep Removal of Toluene by Highly Utilizing Sunlight Energy

Meng Zhang, Guanghui Li, Qiang Li, Jing Chen, Ehiaghe Agbovhimen Elimian, Hongpeng Jia,\* and Hong He\*



Cite This: *Environ. Sci. Technol.* 2023, 57, 4286–4297



Read Online

ACCESS |

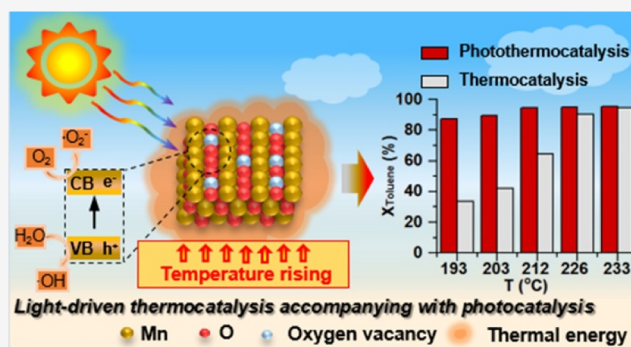
Metrics & More

Article Recommendations

Supporting Information

**ABSTRACT:** The alternative use of electric energy by renewable energy to supply power for catalytic oxidation of pollutants is a sustainable technology, requiring a competent catalyst to realize efficient utilization of light and drive the catalytic reaction. Herein, in situ-synthesized manganese oxide heterostructure composites are developed through solvothermal reduction and subsequent calcination of amorphous manganese oxide (AMO). 95% of toluene conversion and 80% of CO<sub>2</sub> mineralization were achieved over amorphous manganese oxide calcined at 250 °C (AMO-250) under light irradiation, and catalyst stability was maintained for at least 40 h. Highly utilization of light energy, uniformly dispersed nanoparticles, large specific surface area, improved metal reducibility, and oxygen desorption and migration ability at low temperature contribute to the good catalytic oxidation activity of AMO-250. Light activated more lattice oxygen to participate in the reaction via the Mars–van Krevelen (MvK) mechanism, and traditional e<sup>-</sup>–h<sup>+</sup> photocatalytic behavior exists over the AMO-250 heterostructure composite as an auxiliary degradation path. The reaction pathways of photothermocatalysis and thermocatalysis are close, except for the emergence of different copolymers, where light enhances the deep conversion of intermediates. A proof-of-concept study under natural sunlight has confirmed the feasibility of practical application in the photothermocatalytic degradation of pollutants.

**KEYWORDS:** photothermocatalytic oxidation, VOCs, manganese oxides, sunlight energy, natural sunlight



## 1. INTRODUCTION

Volatile organic compounds (VOCs) emitted from anthropogenic and natural sources come into human living space and endanger human health. Moreover, VOCs are major precursors leading to ozone and secondary organic aerosols in the atmosphere.<sup>1–3</sup> Human yearning for good living space has driven the development of air pollution elimination technology. For VOCs with low concentration and flow rate, photocatalysis and catalytic oxidation are effective degradation methods.<sup>4–6</sup> However, for the degradation of aromatic compounds, such as toluene, they still suffer from low quantum efficiency and high energy consumption, respectively, which make it essential to find a good way that integrates multiple advantages to handle pollutants.<sup>7</sup> Photothermocatalysis makes use of infrared heating and the nonradiative thermal effect generated by the photon coupling to provide power for the catalytic reaction. Based on the special design of photothermocatalysts, (2–8) × sun irradiation (1 × sun = 1 kW·m<sup>-2</sup>) can be effectively exploited to make the catalyst reach the required temperature for reaction through light absorption and light-to-heat conversion. Photothermocatalysts applied in VOC removal are mainly developed based on thermal catalysts,

including noble metal-based catalysts and transition-metal oxide catalysts. Photothermal catalytic oxidation of VOCs has been verified on a variety of catalysts, such as TiO<sub>2</sub>/CeO<sub>2</sub>,<sup>8</sup> MnO<sub>x</sub>/TiO<sub>2</sub>,<sup>9</sup> CeMn<sub>x</sub>O<sub>y</sub>/TiO<sub>2</sub>,<sup>10</sup> Pt/CuO–CeO<sub>2</sub>,<sup>11</sup> and Pt/CeO<sub>2</sub>/TiO<sub>2</sub>,<sup>12</sup> as a catalytic process where the comprehensive effects of photocatalysis and thermocatalysis work together to promote the catalytic reaction. Our previous work has also proved that light not only acts as a heat source but also activates more lattice oxygen to participate in the reaction, while photocatalysis plays an auxiliary role.<sup>13,14</sup>

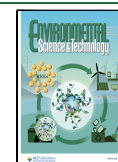
To effectively improve photocatalytic activity, heterojunction engineering has been regarded as an appealing strategy to enhance the light absorption of semiconductors and prolong the separation lifetime of photogenerated charge carriers.<sup>15,16</sup> Heterocomplexes on account of transition-metal oxides are

Received: December 3, 2022

Revised: February 16, 2023

Accepted: February 17, 2023

Published: March 1, 2023



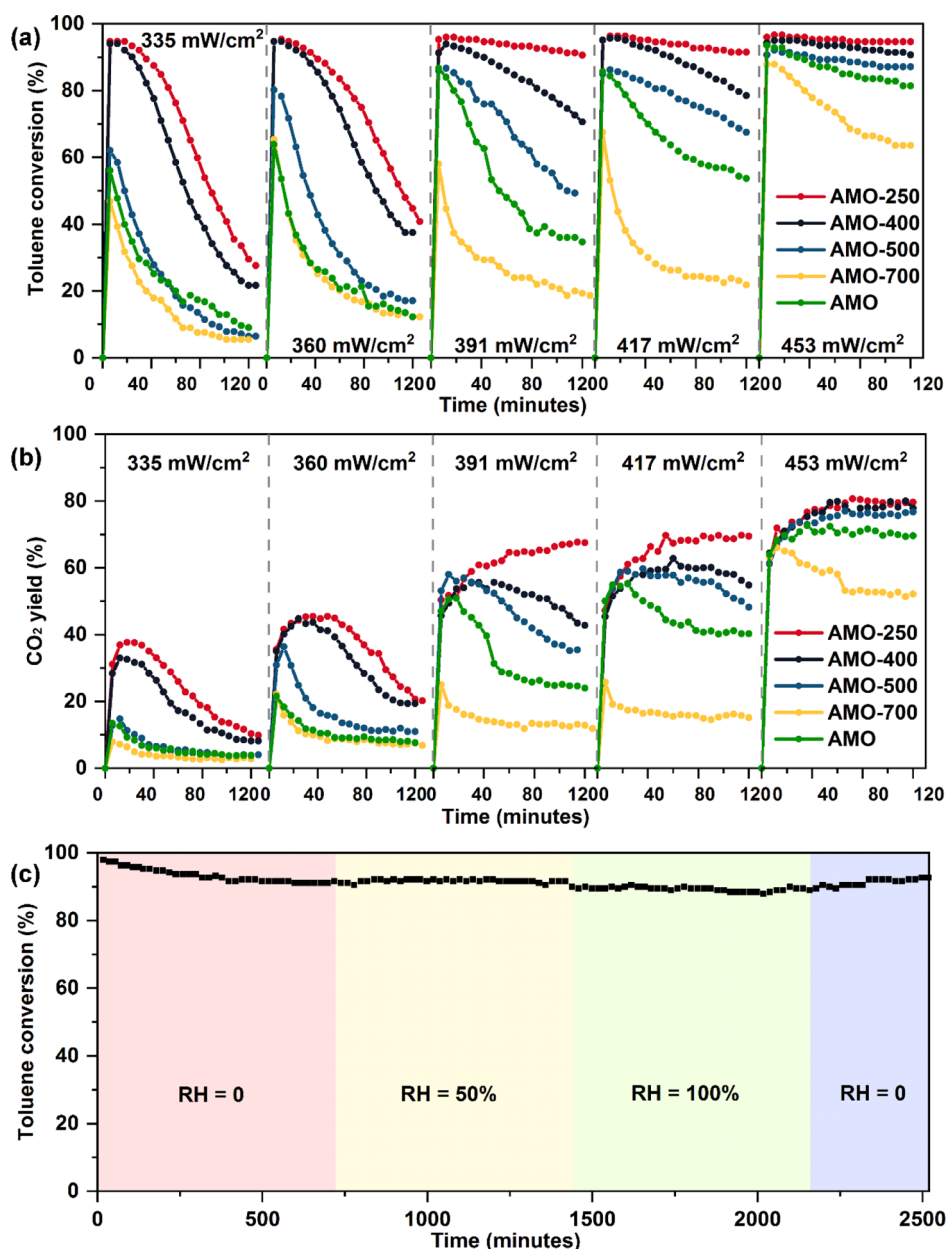


**Figure 1.** (a) Toluene conversion and (b) CO<sub>2</sub> yield over AMO, AMO-250, AMO-400, AMO-500, and AMO-700 under full-spectrum irradiation with varied light intensities (335, 360, 391, 417, and 453 mW/cm<sup>2</sup>). (c) Stability of AMO-250 under dry and humid conditions [relative humidity (RH) = 50 and 100%, respectively] for toluene conversion with a light illumination of 453 mW/cm<sup>2</sup>. Reaction condition: 170 ppm of toluene; 45,000 mL/(g·h).

extensively applied in catalysis due to their reversible valence states and abundant active sites.<sup>17,18</sup> The virtues of manganese oxides have been verified in the field of photocatalysis and thermocatalysis, mainly consisting of several stable metal oxides (MnO, Mn<sub>2</sub>O<sub>3</sub>, Mn<sub>3</sub>O<sub>4</sub>, and MnO<sub>2</sub>), whose oxidation states vary due to their band gap and structural properties.<sup>19–22</sup> In theory, heterostructure composites involving two or more manganese oxides possess the improving separation efficiency of photogenerated charge carriers, abundant catalytic active sites, and good light absorption, thus exhibiting great potential for photothermocatalytic oxidation.

In the present work, a MnO/Mn<sub>3</sub>O<sub>4</sub> heterostructure catalyst with the function of effective light harvesting and abundant active sites is designed and constructed for the photothermocatalytic elimination of toluene. Amorphous manganese

oxide (AMO) was synthesized by solvothermal reduction and subsequent calcination in situ at different temperatures to regulate the structure. The function and the reaction mechanism of heterostructure catalysts in photothermocatalytic degradation of toluene are exclusively investigated. The reaction pathway of thermocatalytic and photothermocatalytic oxidation of toluene over the catalyst is excavated and compared. Furthermore, the degradation of pollutants under natural sunlight is attempted to explore the feasibility of the practical utilization of sunlight.

## 2. EXPERIMENTAL SECTION

**2.1. Chemicals and Reagents.** All chemicals are of analytically pure grade without further purification. Manganese acetate tetrahydrate (Mn(CH<sub>3</sub>COO)<sub>2</sub>·4H<sub>2</sub>O), *n*-octanol, and

Table 1. Summary of Manganese-Based Catalysts for Toluene Catalytic Oxidation Reported in the Literatures

catalyst	concentration (ppm), GHSV(mL/(g h))	light irradiation (mW/cm <sup>2</sup> )	temperature (°C)	toluene conversion (%)	refs
AMO-250	170, 45 000	393	212	90	This work
		453	233	95	
commercial MnO <sub>2</sub>		453	231	86	
9 wt.%MnO <sub>x</sub> -CeO <sub>2</sub>	100, 60 000		210	90	17
CoMn <sub>2</sub> O <sub>4</sub>	500, 22 500		210	90	18
$\alpha$ @ $\beta$ -MnO <sub>2</sub>	500, 30 000		205	100	23
A-LaTi <sub>0.6</sub> Mn <sub>0.4</sub> O <sub>3+<math>\delta</math></sub>	200, 30 000	650	227.5	96	14
MnO <sub>2</sub> -Ac	1000, 90 000		200	90	24
MnO <sub>x</sub> -ET	1000, 60 000		225	90	25
MnO <sub>2</sub> /LaMnO <sub>3</sub>	2000, 120 000		279	90	20
$\alpha$ -MnO <sub>2</sub> /Mn <sub>3</sub> O <sub>4</sub>	300, 45 000	764	130	90	16
Mn <sub>2</sub> O <sub>3</sub> @MnO <sub>2</sub>	1000, 60 000		252	90	26
Mn <sub>2</sub> O <sub>3</sub>	1000, 60 000		239	90	27
MnO <sub>x</sub>	500, 60 000		238	90	21

absolute alcohol were purchased from Sinopharm Chemical Reagent Co., Ltd. Deionized water was used in synthesis experiments.

**2.2. Catalyst Preparation.** Pristine AMO (MnO) was synthesized by a solvothermal method. 4 g of manganese acetate tetrahydrate (Mn(CH<sub>3</sub>COO)<sub>2</sub>·4H<sub>2</sub>O) was dissolved in a mixture of 16 mL of *n*-octanol and 48 mL of ethanol. The solution was stirred for 2 h and then transferred into a 100 mL Teflon-lined stainless-steel autoclave, which was sealed and heated at 220 °C for 4 h. Until the autoclave cooled down to room temperature, the resulting slurry was filtered and washed several times with absolute ethanol. The final product was dried at 100 °C for 8 h and collected. The obtained amorphous MnO was denoted as AMO. The AMO was calcined at 250, 400, 500, and 700 °C under air for 3 h in a tubular furnace and named AMO-250, AMO-400, AMO-500, and AMO-700, respectively.

**2.3. Evaluation of Photothermocatalytic Degradation Activity of Toluene.** The test condition and operation procedures of photothermocatalytic oxidation, photocatalytic oxidation, thermocatalytic oxidation, and the degradation experiment of pollutants under natural sunlight are described in Text S1. The schematic diagram of the photothermal experimental setup is shown in Scheme S1.

**2.4. Catalyst Characterization.** The catalysts were characterized by X-ray diffraction (XRD), thermogravimetry (TG), X-ray photoelectron spectroscopy (XPS), high-resolution transmission electron microscopy, nitrogen adsorption-desorption, UV-vis-IR diffuse reflectance spectroscopy (DRS), oxygen-temperature programmed desorption (O<sub>2</sub>-TPD), hydrogen-temperature programmed reduction (H<sub>2</sub>-TPR) and toluene-temperature programmed desorption (toluene-TPD), toluene-temperature programmed oxidation (toluene-TPO), electron paramagnetic resonance (EPR), and in situ DRIFTS. The detailed characterization process is recorded in Text S2.

### 3. RESULTS AND DISCUSSION

**3.1. Photothermocatalytic Performance for Toluene Degradation.** Figure 1a,b displays the time dependence of toluene degradation and CO<sub>2</sub> production over the catalysts under full spectrum with varied light intensities (335, 360, 391, 417, and 453 mW/cm<sup>2</sup>). Under identical light intensity, the photothermocatalytic activities follow the sequence: AMO-250 > AMO-400 > AMO-500 > AMO > AMO-700. Compared

with the traditional electric heating mode, the layer temperature rises rapidly and reaches equilibrium upon light irradiation due to effective light absorption and light-to-heat conversion (Figure S1). The equilibrium temperature is approximately equal over the catalyst under determined light intensity due to the similar crystal structure and rises along with the increase of light intensities (335, 360, 391, 417, and 453 mW/cm<sup>2</sup>) over each individual catalyst, as displayed in Figure S2. Remarkably, with the elevation of input energy, the temperature and toluene removal efficiency increased. The high light intensity is converted to high temperature over the catalysts, which is the energy source driving the photothermocatalytic reaction, namely, the photothermal effect. Under the light intensities of 335 and 360 mW/cm<sup>2</sup>, the catalysts exhibited a toluene conversion efficiency of more than 90% during the initial reaction time, which then dropped gradually within 120 min. Toluene degradation could remain above 90% with a light intensity higher than 391 mW/cm<sup>2</sup> over AMO-250 when the layer temperature was 212 °C or above. Under irradiation with a light intensity of 453 mW/cm<sup>2</sup>, AMO-250 shows a catalyst layer temperature of 233 °C and presents the best photothermocatalytic performance with a toluene conversion of 95% and a CO<sub>2</sub> mineralization of 80% for at least 120 min compared to the counterparts. Under the same reaction condition, the catalytic activity of commercial MnO<sub>2</sub> is presented in Figure S3, and it displays 86% of toluene conversion and 54% of CO<sub>2</sub> yield at 231 °C. Also, the catalytic activity of the obtained AMO-250 was compared with the other manganese-based catalysts in the literatures, as recorded in Table 1. AMO-250 exhibits advantageous photothermocatalytic performance under light irradiation, even compared with catalysts working under stable electric heating conditions.

Furthermore, the stability of AMO-250 in the continuous photothermocatalytic degradation of toluene was checked under dry and humid conditions at a light intensity of 453 mW/cm<sup>2</sup>, as shown in Figure 1c. In the first 198 min, the toluene conversion dropped from 98 to 92% and then was maintained for at least 12 h. At a 50% relative humidity, the catalyst did not show any deactivation and maintained the degradation efficiency of 92% within another 12 h. When the relative humidity increased to 100%, the toluene conversion decreased and remained at 89% for 12 h because of the competitive adsorption of water and reactant molecules on active centers. At last, after cutting off the water vapor, the photothermocatalytic performance recovered to 92%. As

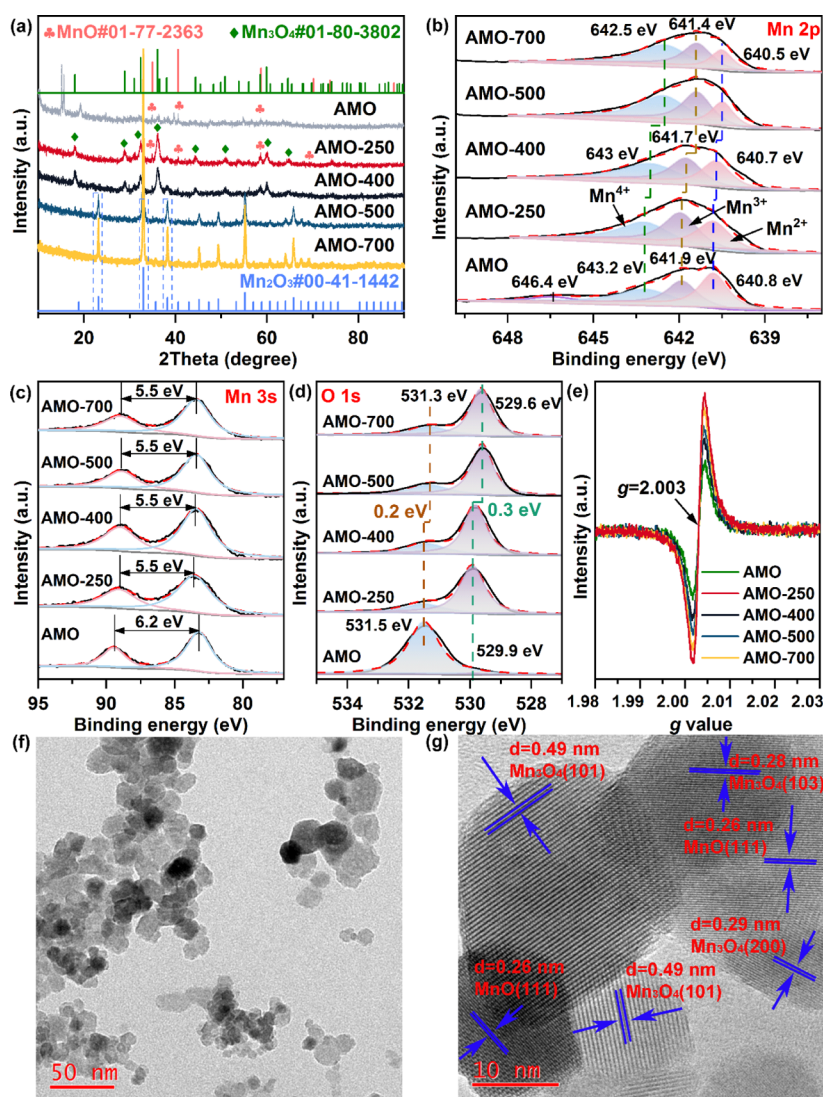


**Figure 2.** (a) XRD patterns and XPS spectra of (b) Mn 2p, (c) Mn 3s, and (d) O 1s of the samples (AMO, AMO-250, AMO-400, AMO-500, and AMO-700), (e) EPR of the samples, and (f–g) HR-TEM images of AMO-250.

displayed in Figure S4, the CO<sub>2</sub> yield increased from 70 to 86% within the first 198 min and then the variation trend was consistent with that of toluene conversion. The CO<sub>2</sub> yield was maintained at 86% within 24 h under dry conditions and 50% relative humidity. At a 100% relative humidity, the CO<sub>2</sub> yield reduced and remained at 73% for 12 h. Finally, after cutting off the water vapor, it was restored to 79% for at least 6 h. Therefore, the AMO-250 catalyst exhibits desirable and long-term stability.

### 3.2. Structural Characterizations of the Catalysts.

XRD patterns associated with crystal structure of the samples are presented in Figure 2a, and AMO is identified as amorphous MnO with poor crystallinity. Since AMO is synthesized in reducing alcohol solvent under high temperature and pressure, its surface contains a large number of organic substances and adsorbed hydroxyl groups. Thermogravimetric analysis was performed within the temperature range of 40–800 °C under air flow, as displayed in Figure S5. The initial weight loss of 1.4% below 170 °C is assigned to the physically adsorbed water species over the catalyst surface, and subsequently, the great weight decrease of 23.4% between 170 and 260 °C is attributed to the combustion and removal of

organic matter.<sup>28</sup> A strong endothermic peak is observed at 258 °C based on the DTG analysis. Subsequently, the slow weight recovery is due to the oxidation reaction process from the low valency to the high valency of manganese oxides. It has been proven that MnO will be transformed into Mn<sub>2</sub>O<sub>3</sub> through a heat treatment above 500 °C in air.<sup>29</sup> As shown in Figure 2a, the calcined samples at 250 and 400 °C comprise MnO and Mn<sub>3</sub>O<sub>4</sub>, which are matched with a cubic structure (JCPDS 77-2363,  $Fm\bar{3}m$ ) and tetragonal structure (JCPDS 80-3802,  $I4_1/amd$ ). For AMO-500 and AMO-700, the crystalline structures were reconstructed and changed into Mn<sub>2</sub>O<sub>3</sub> (JCPDS 41-1442,  $I\bar{4}3$ ). The crystal size of the catalysts was estimated according to the Scherrer formula and is recorded in Table 2 based on the strongest peak in the XRD patterns. The grain size of AMO-250 and AMO-400 is about 14 nm depending on the (211) crystal plane at 36.1° of Mn<sub>3</sub>O<sub>4</sub>. With the elevation of activation temperature, the particle size of AMO-500 and AMO-700 increases to 27 and 43 nm, respectively, owing to the agglomeration of nanoparticles at high temperature.<sup>30,31</sup>

The surface Mn-oxidation state and concentration of oxygen species were detected by XPS, and the data fitting is shown in

Table 2. Physical Structural Properties and Element Components on the Surface and in Bulk

samples	particle size (nm) <sup>a</sup>	$Mn^{2+}/(Mn^{2+}+Mn^{3+}+Mn^{4+})^b$	$Mn^{3+}/(Mn^{2+}+Mn^{3+}+Mn^{4+})^b$	$Mn^{4+}/(Mn^{2+}+Mn^{3+}+Mn^{4+})^b$	$O_{ads}/(O_{ads} + O_{latt})^b$	$S_{BET}$ (m <sup>2</sup> /g) <sup>c</sup>	pore volume (cm <sup>3</sup> /g) <sup>d</sup>	pore diameter (nm) <sup>d</sup>
AMO		0.40	0.29	0.31	0.98	30.56	0.05	3.71
AMO-250	14.59	0.33	0.36	0.31	0.21	60.35	0.29	3.71
AMO-400	14.35	0.31	0.32	0.37	0.24	44.18	0.22	3.71
AMO-500	27.12	0.22	0.35	0.43	0.23	31.11	0.21	3.14
AMO-700	43.39	0.22	0.34	0.44	0.22	19.62	0.08	3.14

<sup>a</sup>The particle size is calculated from Scherrer's equation ( $D = K\lambda/B\cos\theta$ ). <sup>b</sup>The elemental ratios of Mn<sup>2+</sup>, Mn<sup>3+</sup>, and Mn<sup>4+</sup> are calculated according to the fitting peak areas. <sup>c</sup>The specific surface area is calculated by the Brunauer–Emmett–Teller (BET) method. <sup>d</sup>The pore volume and pore diameter are calculated by the Barrett–Joyner–Halenda (BJH) method.

Figure 2b,d and Table 2. Mn 2p is divided into three peaks at 642.5–643.2, 641.4–641.9, and 640.5–640.8 eV, corresponding to Mn<sup>4+</sup>, Mn<sup>3+</sup>, and Mn<sup>2+</sup>, respectively (Figure 1b).<sup>32</sup> The peak at 646.4 eV is a satellite peak only belonging to MnO in the AMO sample. The average oxidation state (AOS) increases after the calcination treatment, which is determined according to the formula  $AOS = 8.96 - 1.13\Delta E$  (the energy gap between the two multiple splitting peaks in Mn 3s) (Figure 2c). Previous research has proved that the  $\Delta E$  for Mn<sup>2+</sup>, Mn<sup>3+</sup>, and Mn<sup>4+</sup> are 6.0, 5.2, and 4.7 eV, respectively.<sup>33–35</sup> As presented in Figure 2c, the  $\Delta E$  of AMO is 6.2 eV, indicating that manganese exists in the form of MnO. In addition, all calcined samples exhibit a  $\Delta E$  of 5.5 eV, confirming the presence of mixed valence states for manganese. The quantitative analysis results of XPS spectra are given in Table 2. High-temperature activation augments the ratio of Mn<sup>4+</sup> and reduces the proportion of Mn<sup>2+</sup> in the samples to maintain a charge balance accompanied by oxygen evolution. In AMO-250 and AMO-400, the proportion of manganese in different valence states is approximately close, which is conducive to the redox process between them ( $Mn^{2+} \leftrightarrow Mn^{3+} \leftrightarrow Mn^{4+}$ ).<sup>36</sup> The O 1s spectra (Figure 2d) were deconvoluted into two peaks at 531.3–531.5 eV and 529.6–529.9 eV, attributed to the adsorbed oxygen and surface lattice oxygen.<sup>35</sup> Obtained by the solvothermal reduction method, the surface of AMO adsorbs a lot of organic substances and hydroxyl groups, resulting in a high ratio of surface-adsorbed oxygen species (Table 2). Calcination treatment reduces the concentration of adsorbed oxygen, and all the calcined samples show an approximate proportion. In addition, the binding energy of lattice oxygen in AMO-250 and AMO-400 displays a positive shift, representative of weak metal–oxygen bond strength.<sup>37,38</sup> Therefore, AMO-250 and AMO-400 have improved oxygen mobility, which is generally considered to be conducive to the formation of oxygen vacancies. EPR was further carried out to give a discussion about oxygen vacancies. As shown in Figure 2e, the signal at  $g = 2.003$  is attributed to oxygen vacancies, and the intensities follow the following sequence: AMO < AMO-400 < AMO-500 < AMO-700 < AMO-250, which is consistent with the ratio of Mn<sup>3+</sup>. Generally, an oxygen vacancy is credited with active sites related to the adsorption and activation of reactant molecules; however, the oxygen vacancy content here is not completely consistent with the catalytic activity, illustrating that the catalytic performance of the catalysts is also affected by other factors. Still, the AMO-250 catalyst exhibiting the best catalytic oxidation activity possesses the highest oxygen vacancy content. Furthermore, the XRD patterns and XPS spectra for fresh and spent catalysts are compared in Figure S6. The results demonstrate that the crystal structure of the used catalyst does not change and the ratio of surface-adsorbed oxygen increases during the catalytic reaction process. The proportion of Mn<sup>2+</sup> is slightly higher than that of Mn<sup>3+</sup> and Mn<sup>4+</sup>.

The morphology information of AMO-250 is demonstrated in Figure 2f and presents uniform nanoparticles with a size of about 14 nm, which is consistent with the results of XRD. Also, the lattice spacings are attributed to the crystal planes of MnO and Mn<sub>3</sub>O<sub>4</sub> (Figure 2g). The nitrogen adsorption–desorption isotherm test results of all samples are depicted as typical type-IV isotherms and H3-type hysteresis loops (Figure S7) corresponding to the mesoporous structure, and the calculated specific surface areas based on Brunauer–Emmett–Teller method are recorded in Table 2. The calcined samples get rid

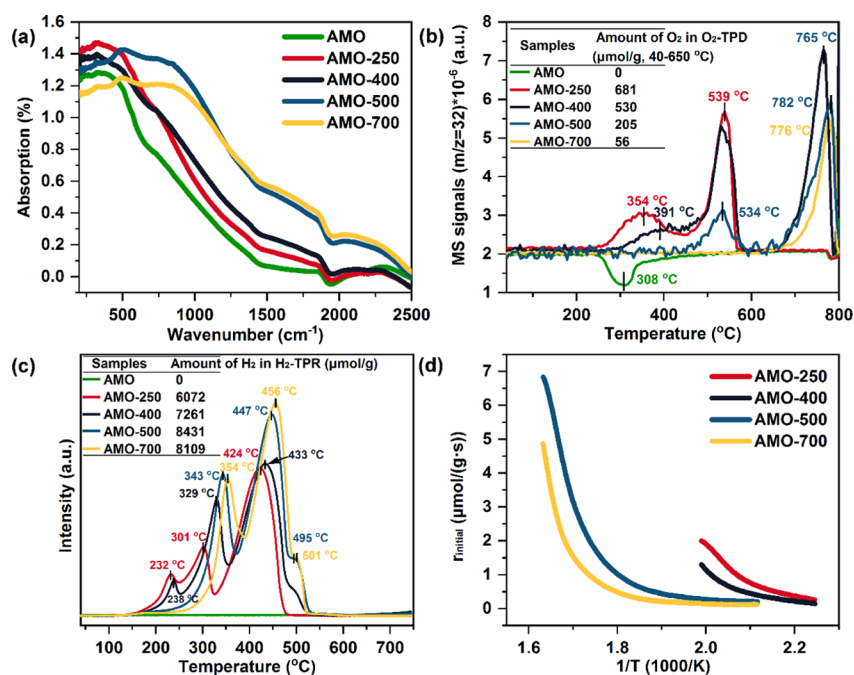


**Figure 3.** (a) UV–vis–IR DRS, (b) O<sub>2</sub>-TPD profiles (inserted table: quantitative analysis of oxygen desorption, 40–650 °C), (c) H<sub>2</sub>-TPR (inserted table: quantitative analysis of hydrogen consumption, 40–700 °C), and (d) initial H<sub>2</sub> consumption rate ( $r_{\text{initial}}$ ) at a low temperature of AMO, AMO-250, AMO-400, AMO-500, and AMO-700.

of the blocking of the organics, thus exhibiting a higher  $S_{\text{BET}}$  than AMO (30.56 m<sup>2</sup>/g). Furthermore, compared with AMO-500 and AMO-700 (31.11 and 19.62 m<sup>2</sup>/g), AMO-250 and AMO-400 possess larger specific surface areas (60.35 and 44.18 m<sup>2</sup>/g) and average pore volume and channel diameter. The elevation of calcination temperature leads to the decrease of specific surface area, which might be mainly due to the increase of particle size and blocking of pores caused by high temperature.<sup>30,39</sup>

**3.3. Optical Absorption and Redox Properties.** During the photothermocatalytic process powered by solar energy, the exploitation of light energy is mainly light absorption and heat conduction by the catalysts. Therefore, it is necessary to investigate the light absorption capacity of the catalyst. As shown in Figure 3a for UV–vis–IR DRS, all the synthesized manganese oxides exhibit good absorption to the majority of the solar spectrum in the wavelength range of 200–1000 nm. Efficient light-to-heat conversion makes the temperature of the catalyst layer elevate to a desirable level, which thus potentially drives the photothermocatalytic reaction to occur. The measured temperatures of AMO, AMO-250, AMO-400, AMO-500, and AMO-700 are close to each other under the same light intensity owing to the approximate light absorption ability (Figure S2).

Chemisorption experiments (H<sub>2</sub>-TPR and O<sub>2</sub>-TPD) were conducted to explore the redox properties of the catalysts. The desorption and mobility ability of oxygen species over the catalysts are investigated by conducting O<sub>2</sub>-TPD (Figure 3b). The desorption order of oxygen species is as follows: (1) physically adsorbed oxygen (<200 °C), (2) chemically adsorbed oxygen (200–400 °C), (3) superficial lattice oxygen (400–600 °C), and (4) lattice oxygen (>600 °C).<sup>40,41</sup> The appearance of an inverted peak at 308 °C over AMO might be due to the reaction between the residual adsorbed organic matter and the trace oxygen in the pipelines as the sample pretreatment temperature in helium only rises to 250 °C.

AMO-250 and AMO-400 demonstrate a lower desorption temperature and higher content of chemically adsorbed oxygen and superficial lattice oxygen, which are the oxygen species mainly involved in the reaction. AMO-700 only shows the desorbed lattice oxygen above 600 °C as a result of the tight metal–oxygen bond caused by high-temperature calcination. The interface synergy in the heterostructure enhances the adsorption of oxygen species, thus facilitating the catalytic oxidation reaction.<sup>26</sup> AMO-250 displays the highest oxygen desorption amount at 40–650 °C, as recorded in the inserted table of Figure 3b, indicating good oxygen desorption and migration capacity. Moreover, the metal reducibility of the catalysts was investigated. As displayed in Figure 3c, the H<sub>2</sub>-TPR profiles of the calcined samples exhibit hydrogen uptake from 150–600 °C, associated with the reduction of manganese oxide composites. Since AMO was obtained by high-temperature solvothermal (ethanol) reduction, it does not consume hydrogen. The desorption of oxygen species by He occurs at a higher temperature than the reduction by hydrogen, attributed to the strong reactivity of hydrogen. AMO-250 presents three reduction peaks located at 232, 301, and 424 °C. The peak centered at 232 and 301 °C is associated with the reduction of Mn<sup>4+</sup> to Mn<sup>3+</sup>, and the peak at 424 °C is attributed to the reduction of Mn<sup>3+</sup> to Mn<sup>2+</sup>.<sup>42,43</sup> The spectrum of AMO-400 shows a similar phenomenon, and the peaks shift to a higher reduction temperature. Three reduction peaks are detected over AMO-500 and AMO-700 at higher temperatures due to the enhancement of the Mn–O bond by high-temperature activation. The formation of a heterostructure also improves the metal reducibility of the catalyst.<sup>23,26</sup> Also, with the calcination activation temperature of the samples elevating, the hydrogen consumption was increased, as presented in the inserted table of Figure 3c, suggesting the reduction of more high-valence manganese in the high-temperature region. Generally, the oxygen species reacting with hydrogen and the metal reducibility at low temperatures are more related to the

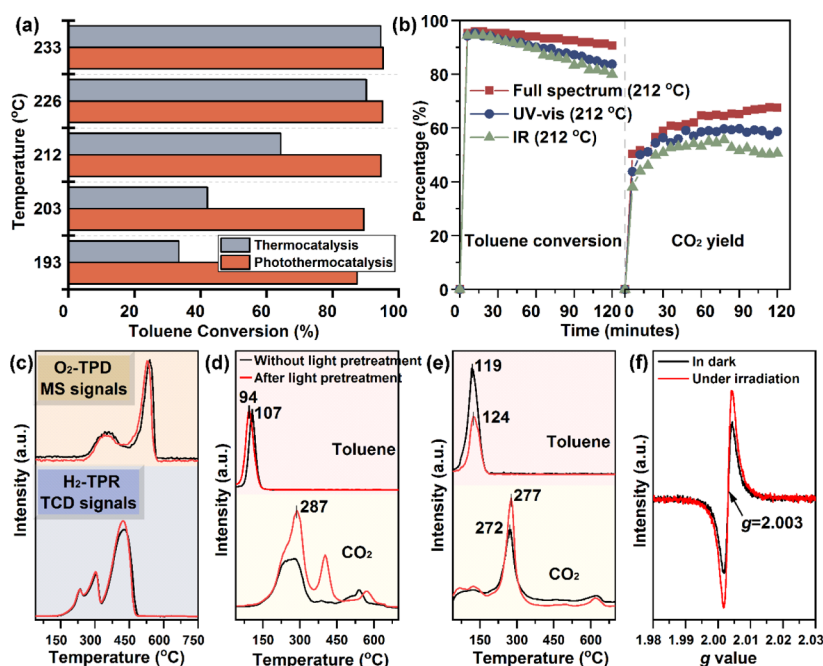


**Figure 4.** (a) Comparison of thermocatalysis and photothermocatalysis for toluene degradation at the determined temperature (193, 203, 212, 226, and 233 °C), (b) toluene conversion and CO<sub>2</sub> yield under different wavelength bands [UV–visible–IR, UV–visible (<700 nm), and IR (>800 nm)] at 212 °C achieved through an optical filter [reaction condition: 170 ppm of toluene, 45,000 mL/(g·h)]. (c) O<sub>2</sub>-TPD and H<sub>2</sub>-TPR, mass spectrum signals (toluene: 92, CO<sub>2</sub>: 44) of toluene-TPD (d) and toluene-TPO (e) after light pretreatment and without light pretreatment over the AMO-250 catalyst, and (f) EPR in the dark and under irradiation.

catalytic performance. Therefore, the H<sub>2</sub> consumption rate at the beginning procedure was calculated according to the differential formula. AMO-250 displays the lowest initial reduction temperature and the highest initial H<sub>2</sub> consumption rate (Figure 3d), thus showing the best catalytic oxidation activity for toluene degradation.

**3.4. Promotive Effect of Light and Photocatalytic Behavior over AMO-250.** The catalytic activities of AMO-250 heterostructure catalysts under full-spectrum irradiation and in dark were evaluated at the same temperature. As demonstrated in Figure 4a, AMO-250 exhibits better photothermocatalytic degradation performance of toluene than thermocatalytic oxidation for at least five temperature points (193, 203, 212, 226, and 233 °C), suggesting that light not only functions as a heat source but also facilitates the catalytic reaction. Besides, the CO<sub>2</sub> yield of photothermocatalysis presents an obvious advantage over thermocatalysis at low temperatures (193, 203, and 212 °C), as exhibited in Figure S8. However, CO<sub>2</sub> production powered by electric heating at 226 °C exceeds that at 233 °C, which might be owing to the deep mineralization of intermediate products accumulated during the continuous heating process. Furthermore, catalytic behaviors at the same temperature (212 °C) at different wavelengths of light are investigated, as displayed in Figure 4b, and the activity order is as follows: UV–visible–IR > UV–visible > IR > electric heating. Light irradiation, especially high-energy UV–vis part (wavelength <700 nm), significantly promotes the catalytic oxidation reaction.

It is well known that the adsorption and activation of reactants (toluene and/or oxygen species) are the pivotal steps during the catalytic oxidation reaction. The influence of light irradiation on the oxygen species over AMO-250 was investigated by comparing the results of O<sub>2</sub>-TPD and H<sub>2</sub>-TPR after light pretreatment and without light pretreatment.

As shown in Figure 4c, the desorption temperature of lattice oxygen shifts to a lower position, and more lattice oxygen is reduced. Thus, more activated lattice oxygen can be produced and participates in the reaction. Also, toluene desorption takes place at a lower temperature of 94 °C after light pretreatment (Figure 4d). Notably, the peak ascribed to CO<sub>2</sub> ( $m/z = 44$ ) appears and starts from 120 °C. Considering no oxygen injection into the system, CO<sub>2</sub> is produced through the reaction between surface lattice oxygen and activated toluene. As manifested in Figure S9, almost no obvious CO<sub>2</sub> signal arises in O<sub>2</sub>-TPD below 350 °C, while a large amount of CO<sub>2</sub> is produced in toluene-TPD, indicating that CO<sub>2</sub> originates from the toluene conversion reaction rather than the adsorbed species on the catalyst surface. As is known, the process of lattice oxygen participating in the catalytic reaction over transition-metal oxides follows the Mars–van Krevelen (MvK) mechanism.<sup>44,45</sup> More CO<sub>2</sub> production in toluene-TPD proves that light promotes the activation of lattice oxygen, thus accelerating the photothermocatalytic reaction activity. In toluene-TPO profiles (Figure 4e), the toluene desorption peak shifts to a higher temperature than in toluene-TPD, implying that the rich oxygen atmosphere promotes the adsorption and activation of toluene on the catalyst. In addition, the toluene desorption amount decreased over the catalyst after light pretreatment, ascribed to the enhanced adsorption of toluene over the more activated lattice oxygen by light irradiation. After light pretreatment, more CO<sub>2</sub> was produced over the AMO-250 catalyst, manifesting that light activates more lattice oxygen to participate in the reaction, thus improving the catalytic oxidation reaction. EPR results (Figure 4f) in the dark and under irradiation reveal that light promotes the generation of oxygen vacancies, which is conducive to the adsorption and activation of reactants.

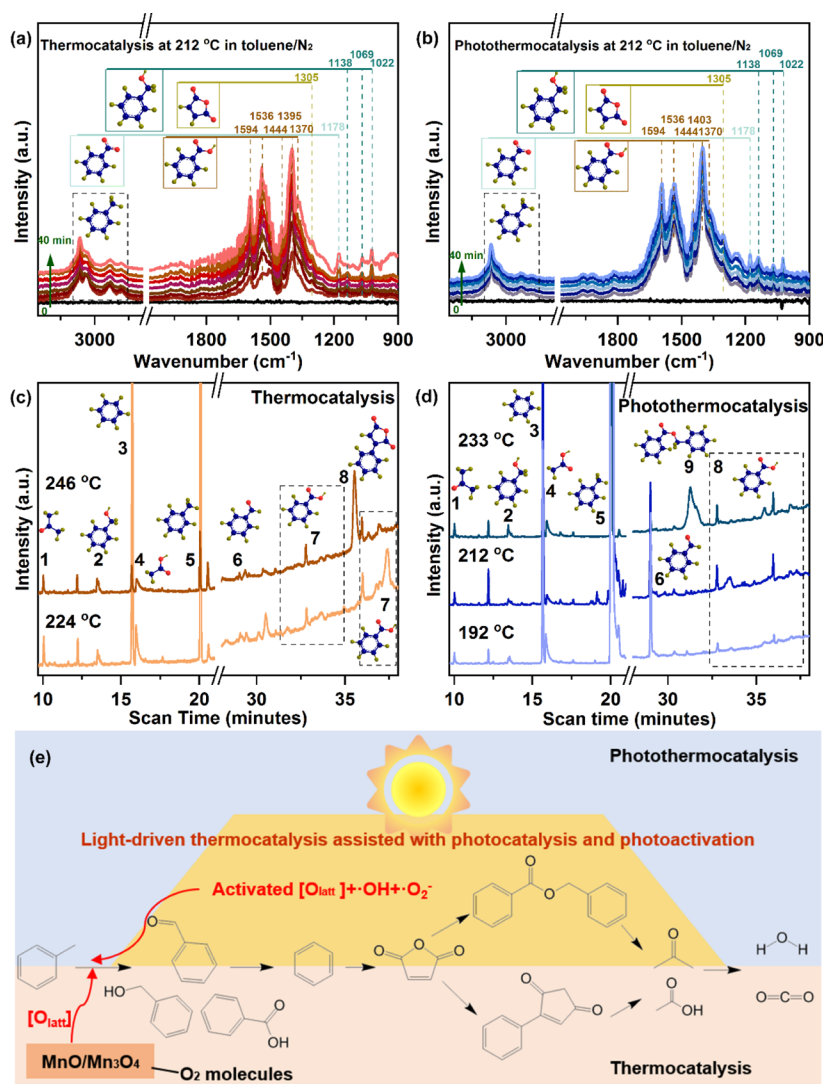


**Figure 5.** In situ DRIFTS spectra of (a) thermocatalytic oxidation and (b) photothermocatalytic oxidation, possible intermediate products detected by GC–MS in the process of (c) thermocatalysis and (d) photothermocatalysis, and (e) reaction mechanism of toluene catalytic oxidation over AMO-250.

In addition, the conventional photocatalytic process over the AMO-250 heterostructure composite was explored. A photocatalytic oxidation experiment eliminating the thermal effect was carried out under an ultraviolet light of 365 nm obtained by filtering the full spectrum with a light intensity of 453 mW/cm<sup>2</sup>. The catalyst layer temperature was 40 °C, and the result demonstrates that the toluene degradation efficiency decreased from 36% to 7% within 2 h without CO<sub>2</sub> production (Figure S10). Therefore, photocatalytic oxidation can only destroy toluene, and high temperature is the crucial factor to promote deep mineralization. The generation of photocurrent over AMO-250 under light irradiation in Figure S11 proves that light excites the semiconductor to produce charge carriers. Furthermore, free radical capture experiments (Figure S12) confirm the generation of reactive oxygen species (DMPO·OH and DMPO·O<sub>2</sub><sup>-</sup>) over AMO-250. Free radicals with strong oxidation ability can effectively initiate chemical reactions. EPR experiments were conducted under heating and irradiation conditions, respectively. As revealed in Figure S12a,d, heating can stimulate the generation of minor superoxide radicals and hydroxyl radicals on the catalyst

surface, while more free radicals are produced when the semiconductor catalyst is activated by light irradiation. Overall, under the condition of both irradiation and heating, most superoxide radicals and hydroxyl radicals arise over the catalyst surface, due to the simultaneous existence of light and heat energy, as shown in Figure S12a,d. Besides, at the same temperature, the full spectrum can stimulate the production of more free radicals than UV–vis or IR illumination, as displayed in Figure S12. The above experiments proved the existence of the photocatalytic process; that is, the heterostructure catalyst is excited by light irradiation to generate electrons and holes and further reacts with other matter (H<sub>2</sub>O, O<sub>2</sub>) to generate strong oxidizing species (·OH and ·O<sub>2</sub><sup>-</sup>). However, photocatalytic degradation is undeniably not the dominant degradation pathway.

**3.5. Reaction Mechanism of Toluene Catalytic Oxidation over AMO-250.** To disclose the reaction pathway of toluene degradation over AMO-250, a series of *in situ* DRIFTS experiments were carried out. Generally, the reaction mechanism follows the MvK mechanism over the reducible transitional-metal oxide.<sup>45</sup> Also, the toluene-TPD experiment

(Figure 4d) has proved that the lattice oxygen of the AMO-250 participates in the reaction. For *in situ* DRIFTS experiments, toluene oxidation was conducted in a N<sub>2</sub> atmosphere to further validate the role of surface lattice oxygen. Prior to the experiments, the catalyst was pretreated in N<sub>2</sub> at 250 °C for 1 h, and then the background and baseline were collected at 212 °C in N<sub>2</sub>. Subsequently, the toluene vapor was introduced by N<sub>2</sub> into the cell and the spectrum was acquired. As displayed in Figure 5a, within 40 min, the peaks of absorbed toluene and derived intermediates were detected gradual enhancement over the catalyst. The peaks at 3066, 3038, 2392, and 2881 cm<sup>-1</sup> are observed, representing the C–H stretch vibration and aromatic ring structure of toluene.<sup>18</sup> The peaks located at 1022, 1069, and 1138 cm<sup>-1</sup> are the characteristics of benzyl alcohol, and the peak centered at 1178 is attributed to the aldehyde species.<sup>11</sup> Benzoate species (1370–1594 cm<sup>-1</sup>) are most evidently formed on AMO-250.<sup>11,18</sup> The band that appeared at 1305 cm<sup>-1</sup> is identified as maleic anhydride.<sup>24,25,27</sup> Comparatively, these peaks also appeared in the photothermocatalytic process (Figure 5b). It is worth mentioning that the *in situ* DRIFTS testing process of photothermocatalysis is consistent with that of thermocatalysis, except that the background and spectrum are collected under the heating condition at 212 °C assisted by light irradiation. The peaks associated with carboxylate appear in both photothermocatalytic and thermocatalytic processes over AMO-250, though the intensities are different. Additionally, more peaks assigned to anhydride species (1305, 1816, 1917, and 1960 cm<sup>-1</sup>) appeared and were observed to be enhanced under light irradiation, indicating the deep oxidation of toluene. A continuous reaction process was performed to observe the promotional effect of light, and the *in situ* DRIFTS spectrum is demonstrated in Figure S13. The background and spectrum of the absorption process were gathered at 35 °C in N<sub>2</sub>, and then the reactor was closed and the reaction temperature was increased to 212 °C. The peaks at 3038, 2881, and 1600 cm<sup>-1</sup> are assigned to the aromatic ring of toluene.<sup>24</sup> Thereafter, toluene was converted into other carbonaceous species with the temperature rising to 212 °C, such as benzaldehyde (1178 cm<sup>-1</sup>) and benzoic acid (1594, 1536, 1395 cm<sup>-1</sup>). Then, light irradiation with a light intensity of 391 mW/cm<sup>2</sup> was introduced into the cell. The peaks ascribed to benzoic acid showed changes in intensity, and the peaks corresponding to anhydride species (1315 cm<sup>-1</sup>) were enhanced, implying the promotional effect of light on the catalytic reaction. At last, air was introduced into the cell for 3 min to supplement oxygen species for the reaction; according to the MvK mechanism, the peaks of most intermediates were observed to weaken and disappeared. Besides, the reaction products during the oxidation process were collected, separated, and then identified by GC–MS, as displayed in Figure 5c,d. The products detected in both photothermocatalytic and thermocatalytic processes include acetone (1), benzyl alcohol (2), benzene (3), acetic acid (4), toluene (5), benzaldehyde (6), and benzoic acid (7). Significantly, phenylmaleic anhydride (8) and benzyl benzoate (9) were, respectively, collected from the exhaust gas of the thermocatalytic reaction at 246 °C and the photothermocatalytic reaction at 233 °C, originating from the polycondensation and esterification reaction. Therefore, light promotes the catalytic reaction process and the reaction pathway for the catalytic oxidation of toluene over AMO-250 follows toluene → benzyl alcohol → benzaldehyde → benzoic acid → benzene →

anhydride → acetone, acetic acid → CO<sub>2</sub>, H<sub>2</sub>O, as shown in Figure 5e. Generally, toluene oxidation begins with the dissociation of a hydrogen atom from the methyl group (–CH<sub>3</sub>) and the formation of benzyl species since the dissociation energy in primary C–H bonds is less than that in terminal methyl groups. Moreover, in the toluene-TPD and toluene-TPO profiles (Figure S14), intermediates including benzene, benzyl alcohol, benzaldehyde, benzoic acid, and maleic anhydride were also detected by mass spectrometry.

**3.6. Photothermocatalytic Oxidation of Toluene Powered by Outdoor Natural Sunlight.** To verify the feasibility of photothermocatalytic toluene degradation experiments powered by the outdoor natural sunlight, a portion of gas pipelines and connected quartz reactor were moved out and placed outdoors. The natural light intensity is about 60 mW/cm<sup>2</sup> between 12:20 and 14:40 on a sunny day (September 30th, 2022). The light intensity was recorded, as shown in Figure 6a, and labeled as a blue dot. An optical

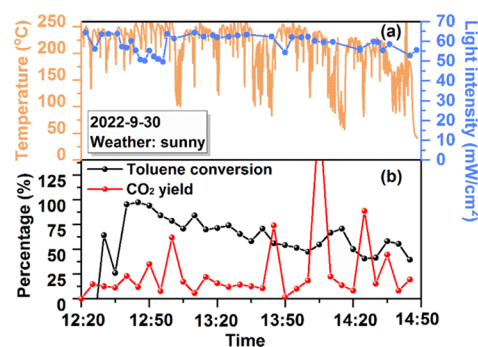


**Figure 6.** (a) Variation of solar radiation intensity (yellow line) and layer temperature obtained by focusing on the catalyst with the Fresnel lens (blue line) from 12:20–14:40 on Sept. 30, 2022, in Xiamen City, China. (b) Simultaneous evolution of toluene conversion and CO<sub>2</sub> yield over AMO-250. Reaction conditions: 170 ppm of toluene, 20 mg of catalyst, GHSV = 45,000 mL/(g·h).

Fresnel lens with a diameter of 90 mm is used to focus sunlight on the catalyst to provide energy for the reaction and the temperature of the catalyst layer after focusing is shown and labeled as a yellow line in Figure 6a. Although available solar irradiance is weak in autumn under low solar elevation, with the help of a condenser, the catalyst layer can still achieve a high temperature at about 230 °C through light absorption and heat conduction. After 14:00, the sun slanted westward, and the solar energy began to spread out, accounting for the drop in temperature.<sup>46–48</sup> Geographically, the solar radiation intensity decreases along with the decline in solar altitude angle. As displayed in Figure 6b, above 50% of toluene conversion and about 10% of CO<sub>2</sub> mineralization were continuously maintained over AMO-250. Since light is focused on the catalyst by manually adjusting the concentrator, the temperature of the catalyst layer fluctuates in a wide range, resulting in an instantaneous large amount of CO<sub>2</sub> emission during the adjustment process. According to the working principle of the condenser, we know that the focused beam forms a very small aperture in the focal plane so as to gather enough energy in the sunlight. The small aperture can only heat part of the catalyst, and then the heat will be conducted on the rest of the metal oxide. Inhomogeneous heating mode results in the inhibition of deep mineralization. Significantly, outdoor experiments validate that the practical application of

natural light on the photothermocatalytic oxidation of toluene is still very promising. Through further design and manufacture of natural light tracking and collection equipment, we will be able to achieve pollutant elimination without external input energy.

**3.7. Environmental Implications.** VOCs are important precursors for the formation of ozone and secondary aerosols, and their own toxicity is harmful to the environment and human health. Catalytic oxidation relying on the catalyst is an effective technology to achieve efficient and stable pollutant degradation with less energy consumption. However, continuous electric energy heating is required to supply power for the catalytic reaction. Especially, for the removal of aromatic hydrocarbon pollutants, external heating needs to provide a high temperature above 150 °C to maintain a stable catalytic reaction. Therefore, renewable energy is expected to replace the traditional electric heating method to supply energy for the degradation of pollutants. The efficient use of sunlight to realize the catalytic degradation of VOCs is an effective and energy-saving way to deal with the pollutants in the environment, in which the key is the delicate design of photothermocatalysts. In this work, a MnO/Mn<sub>3</sub>O<sub>4</sub> heterostructure catalyst was synthesized by the solvothermal method and subsequent calcination. AMO-250 exhibits strong light absorption ability and light-to-heat conversion, and achieves better photothermocatalytic performance than the counterpart catalysts, attributed to the large specific surface area, improved oxygen migration, and metal reducibility. Photothermocatalytic oxidation exhibits better degradation efficiency at least five temperature points than conventional catalytic oxidation, and UV-vis and IR irradiation have a comprehensive effect on promoting the photothermocatalytic activity. The catalytic reaction over AMO-250 follows the MvK mechanism and photo activates more lattice oxygen involved in the reaction, thus improving the catalytic oxidation activity. Also, photocatalysis exists as an auxiliary pathway during the photothermal process. The semiconductor catalyst is excited by light irradiation to generate electrons (e<sup>-</sup>) and holes (h<sup>+</sup>), which further react with oxygen and water to produce reactive oxygen species ( $\cdot\text{O}_2^-$  and  $\cdot\text{OH}$ ) to participate in the reaction. Overall, photothermocatalytic oxidation of toluene over AMO-250 is a photodriven thermocatalytic reaction, accompanied by the photoactivation of lattice oxygen and photocatalytic process, where lattice oxygen and reactive oxygen species ( $\cdot\text{O}_2^-$  and  $\cdot\text{OH}$ ) are the main active oxygen species. The reaction pathways of photothermocatalysis and thermocatalysis are roughly the same, except for the appearance of different copolymers (benzyl benzoate and phenylmaleic anhydride). The catalytic degradation of toluene under natural sunlight over AMO-250 endows great potential in the application of photothermocatalytic oxidation in VOC removal, while the equipment for collection and utilization of light energy still needs further exploration and improvement.

## ■ ASSOCIATED CONTENT

### SI Supporting Information

The Supporting Information is available free of charge at <https://pubs.acs.org/doi/10.1021/acs.est.2c09136>.

Experimental details and figures displaying schematic diagrams of experimental devices, temperature variation with time under light irradiation, layer temperatures under light irradiation, stability for CO<sub>2</sub> yield, TGA of

AMO, XRD patterns and XPS profiles of fresh and spent AMO-250, N<sub>2</sub> adsorption-desorption isotherms, activity comparison of thermocatalysis and photothermocatalysis for CO<sub>2</sub> yield, signal comparison in O<sub>2</sub>-TPD and toluene-TPD profiles, photocatalytic activity over AMO-250 under UV light irradiation of 365 nm, photocurrent spectra, EPR spectra of DMPO-OH and DMPO- $\cdot\text{O}_2^-$  under light and heating conditions over AMO-250, in situ DRIFTS spectra, and on-line mass spectrum signals (PDF)

## ■ AUTHOR INFORMATION

### Corresponding Authors

**Hongpeng Jia** – Xiamen Key Laboratory of Materials for Gaseous Pollutant Control, Institute of Urban Environment, Chinese Academy of Sciences, Xiamen 361021, China; CAS Center for Excellence in Regional Atmospheric Environment, Institute of Urban Environment, Chinese Academy of Sciences, Xiamen, Fujian 361021, China; University of Chinese Academy of Sciences, Beijing 100049, China; [orcid.org/0000-0001-9558-5563](https://orcid.org/0000-0001-9558-5563); Email: [hpjia@iue.ac.cn](mailto:hpjia@iue.ac.cn)

**Hong He** – CAS Center for Excellence in Regional Atmospheric Environment, Institute of Urban Environment, Chinese Academy of Sciences, Xiamen, Fujian 361021, China; University of Chinese Academy of Sciences, Beijing 100049, China; Research Center for Eco-Environmental Sciences, Chinese Academy of Sciences, Beijing 100085, China; [orcid.org/0000-0001-8476-8217](https://orcid.org/0000-0001-8476-8217); Phone: 86-592-6190767; Email: [honghe@rcees.ac.cn](mailto:honghe@rcees.ac.cn); Fax: 86-592-6190767

### Authors

**Meng Zhang** – Xiamen Key Laboratory of Materials for Gaseous Pollutant Control, Institute of Urban Environment, Chinese Academy of Sciences, Xiamen 361021, China; CAS Center for Excellence in Regional Atmospheric Environment, Institute of Urban Environment, Chinese Academy of Sciences, Xiamen, Fujian 361021, China; University of Chinese Academy of Sciences, Beijing 100049, China

**Guanghui Li** – Xiamen Key Laboratory of Materials for Gaseous Pollutant Control, Institute of Urban Environment, Chinese Academy of Sciences, Xiamen 361021, China; CAS Center for Excellence in Regional Atmospheric Environment, Institute of Urban Environment, Chinese Academy of Sciences, Xiamen, Fujian 361021, China; College of Environment and Safety Engineering, Fuzhou University, Fuzhou, Fujian 350108, China

**Qiang Li** – Xiamen Key Laboratory of Materials for Gaseous Pollutant Control, Institute of Urban Environment, Chinese Academy of Sciences, Xiamen 361021, China; CAS Center for Excellence in Regional Atmospheric Environment, Institute of Urban Environment, Chinese Academy of Sciences, Xiamen, Fujian 361021, China; University of Chinese Academy of Sciences, Beijing 100049, China

**Jing Chen** – Xiamen Institute of Rare-earth Materials, Haixi Institutes, Chinese Academy of Sciences, Xiamen, Fujian 361021, China; University of Chinese Academy of Sciences, Beijing 100049, China; [orcid.org/0000-0001-9298-2651](https://orcid.org/0000-0001-9298-2651)

**Ehiaghe Agbovhimen Elimian** – Xiamen Key Laboratory of Materials for Gaseous Pollutant Control, Institute of Urban Environment, Chinese Academy of Sciences, Xiamen 361021, China; CAS Center for Excellence in Regional Atmospheric

Environment, Institute of Urban Environment, Chinese Academy of Sciences, Xiamen, Fujian 361021, China; Department of Chemical and Environmental Engineering, Faculty of Science and Engineering, University of Nottingham, Ningbo, Zhejiang 315100, China

Complete contact information is available at:  
<https://pubs.acs.org/10.1021/acs.est.2c09136>

## Notes

The authors declare no competing financial interest.

## ACKNOWLEDGMENTS

This work was supported by the National Key Research and Development Program of China (no. 2022YFB3504200); Xiamen Science and Technology Plan Project (no. 3502Z20226022); the National Nature Science Foundation of China (nos. 21976172 and 22176187); the Science and Technology Planning Project of Fujian Province (no. 2020Y0084); and the Youth Innovation Promotion Association of CAS [no. 2021304].

## REFERENCES

- (1) Huang, X.-F.; Cao, L.-M.; Tian, X.-D.; Zhu, Q.; Saikawa, E.; Lin, L.-L.; Cheng, Y.; He, L.-Y.; Hu, M.; Zhang, Y.-H.; Lu, K.-D.; Liu, Y.-H.; Daellenbach, K.; Slowik, J. G.; Tang, Q.; Zou, Q.-L.; Sun, X.; Xu, B.-Y.; Jiang, L.; Shen, Y.-M.; Ng, N. L.; Prévôt, A. S. H. Critical Role of Simultaneous Reduction of Atmospheric Odd Oxygen for Winter Haze Mitigation. *Environ. Sci. Technol.* **2021**, *55*, 11557–11567.
- (2) Trueblood, J. V.; Wang, X.; Or, V. W.; Alves, M. R.; Santander, M. V.; Prather, K. A.; Grassian, V. H. The Old and the New: Aging of Sea Spray Aerosol and Formation of Secondary Marine Aerosol through OH Oxidation Reactions. *ACS Earth Space Chem* **2019**, *3*, 2307–2314.
- (3) Xu, B.; Zhang, G.; Gustafsson, Ö.; Kawamura, K.; Li, J.; Andersson, A.; Bikkina, S.; Kunwar, B.; Pokhrel, A.; Zhong, G.; Zhao, S.; Li, J.; Huang, C.; Cheng, Z.; Zhu, S.; Peng, P.; Sheng, G. Large contribution of fossil-derived components to aqueous secondary organic aerosols in China. *Nat. Commun.* **2022**, *13*, 5115.
- (4) He, F.; Weon, S.; Jeon, W.; Chung, M. W.; Choi, W. Self-wetting triphase photocatalysis for effective and selective removal of hydrophilic volatile organic compounds in air. *Nat. Commun.* **2021**, *12*, 6259.
- (5) Chen, C.; Li, Y.; Yang, Y.; Zhang, Q.; Wu, J.; Xie, X.; Shi, Z.; Zhao, X. Unique mesoporous amorphous manganese iron oxide with excellent catalytic performance for benzene abatement under UV-vis-IR and IR irradiation. *Environ. Sci.: Nano* **2019**, *6*, 1233–1245.
- (6) Li, Q.; Luo, N.; Xia, D.; Huang, P.; Liu, X.; Odoom-Wubah, T.; Huang, J.; Chai, G.; Sun, D.; Li, Q. Interfacial effects in CuO/Co<sub>3</sub>O<sub>4</sub> heterostructures enhance benzene catalytic oxidation performance. *Environ. Sci.: Nano* **2022**, *9*, 781–796.
- (7) Wu, P.; Jin, X.; Qiu, Y.; Ye, D. Recent Progress of Thermocatalytic and Photo/Thermocatalytic Oxidation for VOCs Purification over Manganese-based Oxide Catalysts. *Environ. Sci. Technol.* **2021**, *55*, 4268–4286.
- (8) Zeng, M.; Li, Y.; Mao, M.; Bai, J.; Ren, L.; Zhao, X. Synergetic Effect between Photocatalysis on TiO<sub>2</sub> and Thermocatalysis on CeO<sub>2</sub> for Gas-Phase Oxidation of Benzene on TiO<sub>2</sub>/CeO<sub>2</sub> Nanocomposites. *ACS Catal.* **2015**, *5*, 3278–3286.
- (9) Lan, L.; Li, Y.; Zeng, M.; Mao, M.; Ren, L.; Yang, Y.; Liu, H.; Yun, L.; Zhao, X. Efficient UV-vis-infrared light-driven catalytic abatement of benzene on amorphous manganese oxide supported on anatase TiO<sub>2</sub> nanosheet with dominant {001} facets promoted by a photothermocatalytic synergetic effect. *Appl. Catal., B* **2017**, *203*, 494–504.
- (10) Liu, H.; Li, Y.; Yang, Y.; Mao, M.; Zeng, M.; Lan, L.; Yun, L.; Zhao, X. Highly efficient UV-Vis-infrared catalytic purification of benzene on CeMn<sub>2</sub>O<sub>7</sub>/TiO<sub>2</sub> nanocomposite, caused by its high thermocatalytic activity and strong absorption in the full solar spectrum region. *J. Mater. Chem. A* **2016**, *4*, 9890–9899.
- (11) Feng, Y.; Dai, L.; Wang, Z.; Peng, Y.; Duan, E.; Liu, Y.; Jing, L.; Wang, X.; Rastegarpanah, A.; Dai, H.; Deng, J. Photothermal Synergistic Effect of Pt<sub>1</sub>/CuO-CeO<sub>2</sub> Single-Atom Catalysts Significantly Improving Toluene Removal. *Environ. Sci. Technol.* **2022**, *56*, 8722–8732.
- (12) Feng, Y.; Ma, P.; Wang, Z.; Shi, Y.; Wang, Z.; Peng, Y.; Jing, L.; Liu, Y.; Yu, X.; Wang, X.; Zhang, X.; Deng, J.; Dai, H. Synergistic Effect of Reactive Oxygen Species in Photothermocatalytic Removal of VOCs from Cooking Oil Fumes over Pt/CeO<sub>2</sub>/TiO<sub>2</sub>. *Environ. Sci. Technol.* **2022**, *56*, 17341–17351.
- (13) Li, J.; Zhang, M.; Elimian, E. A.; Lv, X.; Chen, J.; Jia, H. Convergent ambient sunlight-powered multifunctional catalysis for toluene abatement over in situ exsolution of Mn<sub>3</sub>O<sub>4</sub> on perovskite parent. *Chem. Eng. J.* **2021**, *412*, 128560.
- (14) Yu, E.; Chen, J.; Jia, H. Enhanced light-driven photothermocatalytic activity on selectively dissolved LaTi<sub>1-x</sub>Mn<sub>x</sub>O<sub>3+δ</sub> perovskites by photoactivation. *J. Hazard. Mater.* **2020**, *399*, 122942.
- (15) Kumar, P.; Laishram, D.; Sharma, R. K.; Vinu, A.; Hu, J.; Kibria, M. G. Boosting Photocatalytic Activity Using Carbon Nitride Based 2D/2D van der Waals Heterojunctions. *Chem. Mater.* **2021**, *33*, 9012–9092.
- (16) Wu, P.; Dai, S.; Chen, G.; Zhao, S.; Xu, Z.; Fu, M.; Chen, P.; Chen, Q.; Jin, X.; Qiu, Y.; Yang, S.; Ye, D. Interfacial effects in hierarchically porous α-MnO<sub>2</sub>/Mn<sub>3</sub>O<sub>4</sub> heterostructures promote photocatalytic oxidation activity. *Appl. Catal., B* **2020**, *268*, 118418.
- (17) Cao, Y.; Zhang, C.; Xu, D.; Ouyang, X.; Wang, Y.; Lv, L.; Zhang, T.; Tang, S.; Tang, W. Low-Temperature Oxidation of Toluene over MnO<sub>x</sub>-CeO<sub>2</sub> Nanorod Composites with High Sinter Resistance: Dual Effect of Synergistic Interaction on Hydrocarbon Adsorption and Oxygen Activation. *Inorg. Chem.* **2022**, *61*, 15273–15286.
- (18) Dong, C.; Qu, Z.; Qin, Y.; Fu, Q.; Sun, H.; Duan, X. Revealing the Highly Catalytic Performance of Spinel CoMn<sub>2</sub>O<sub>4</sub> for Toluene Oxidation: Involvement and Replenishment of Oxygen Species Using In Situ Designed-TP Techniques. *ACS Catal.* **2019**, *9*, 6698–6710.
- (19) Wang, H.; Huang, Z.; Jiang, Z.; Zhang, Y.; Zhang, Z.; Shangguan, W. Trifunctional C@MnO Catalyst for Enhanced Stable Simultaneously Catalytic Removal of Formaldehyde and Ozone. *ACS Catal.* **2018**, *8*, 3164–3180.
- (20) Si, W.; Wang, Y.; Zhao, S.; Hu, F.; Li, J. A Facile Method for In Situ Preparation of the MnO<sub>2</sub>/LaMnO<sub>3</sub> Catalyst for the Removal of Toluene. *Environ. Sci. Technol.* **2016**, *50*, 4572–4578.
- (21) Zhang, X.; Ma, Z. a.; Song, Z.; Zhao, H.; Liu, W.; Zhao, M.; Zhao, J. Role of Cryptomelane in Surface-Adsorbed Oxygen and Mn Chemical Valence in MnO<sub>x</sub> during the Catalytic Oxidation of Toluene. *J. Phys. Chem. C* **2019**, *123*, 17255–17264.
- (22) Pan, H.; Jian, Y.; Chen, C.; He, C.; Hao, Z.; Shen, Z.; Liu, H. Sphere-Shaped Mn<sub>3</sub>O<sub>4</sub> Catalyst with Remarkable Low-Temperature Activity for Methyl–Ethyl–Ketone Combustion. *Environ. Sci. Technol.* **2017**, *51*, 6288–6297.
- (23) Huang, N.; Qu, Z.; Dong, C.; Qin, Y.; Duan, X. Superior performance of α/β-MnO<sub>2</sub> for the toluene oxidation: Active interface and oxygen vacancy. *Appl. Catal., A* **2018**, *560*, 195–205.
- (24) Lyu, Y.; Li, C.; Du, X.; Zhu, Y.; Zhang, Y.; Li, S. Catalytic oxidation of toluene over MnO<sub>2</sub> catalysts with different Mn (II) precursors and the study of reaction pathway. *Fuel* **2020**, *262*, 116610.
- (25) Mo, S.; Zhang, Q.; Li, J.; Sun, Y.; Ren, Q.; Zou, S.; Zhang, Q.; Lu, J.; Fu, M.; Mo, D.; Wu, J.; Huang, H.; Ye, D. Highly efficient mesoporous MnO<sub>2</sub> catalysts for the total toluene oxidation: Oxygen-Vacancy defect engineering and involved intermediates using in situ DRIFTS. *Appl. Catal., B* **2020**, *264*, 118464.
- (26) Yang, W.; Peng, Y.; Wang, Y.; Wang, Y.; Liu, H.; Su, Z. a.; Yang, W.; Chen, J.; Si, W.; Li, J. Controllable redox-induced in-situ growth of MnO<sub>2</sub> over Mn<sub>2</sub>O<sub>3</sub> for toluene oxidation: Active heterostructure interfaces. *Appl. Catal., B* **2020**, *278*, 119279.

- (27) Yang, X.; Yu, X.; Lin, M.; Ma, X.; Ge, M. Enhancement effect of acid treatment on  $\text{Mn}_2\text{O}_3$  catalyst for toluene oxidation. *Catal. Today* **2019**, *327*, 254–261.
- (28) Liu, Z.-h.; Ooi, K.; Kanoh, H.; Tang, W.; Yang, X.; Tomida, T. Synthesis of Thermally Stable Silica-Pillared Layered Manganese Oxide by an Intercalation/Solvothermal Reaction. *Chem. Mater.* **2001**, *13*, 473–478.
- (29) Guo, S.; Lu, G.; Qiu, S.; Liu, J.; Wang, X.; He, C.; Wei, H.; Yan, X.; Guo, Z. Carbon-coated  $\text{MnO}$  microparticulate porous nanocomposites serving as anode materials with enhanced electrochemical performances. *Nano Energy* **2014**, *9*, 41–49.
- (30) Yu, Y.; Liu, S.; Ji, J.; Huang, H. Amorphous  $\text{MnO}_2$  surviving calcination: an efficient catalyst for ozone decomposition. *Catal. Sci. Technol.* **2019**, *9*, 5090–5099.
- (31) Ren, Z.; Zhang, H.; Wang, G.; Pan, Y.; Yu, Z.; Long, H. Effect of Calcination Temperature on the Activation Performance and Reaction Mechanism of Ce–Mn–Ru/ $\text{TiO}_2$  Catalysts for Selective Catalytic Reduction of NO with  $\text{NH}_3$ . *ACS Omega* **2020**, *5*, 33357–33371.
- (32) Rong, S.; Zhang, P.; Yang, Y.; Zhu, L.; Wang, J.; Liu, F.  $\text{MnO}_2$  Framework for Instantaneous Mineralization of Carcinogenic Airborne Formaldehyde at Room Temperature. *ACS Catal.* **2017**, *7*, 1057–1067.
- (33) Toupin, M.; Brousse, T.; Bélanger, D. Charge Storage Mechanism of  $\text{MnO}_2$  Electrode Used in Aqueous Electrochemical Capacitor. *Chem. Mater.* **2004**, *16*, 3184–3190.
- (34) Biesinger, M. C.; Payne, B. P.; Grosvenor, A. P.; Lau, L. W. M.; Gerson, A. R.; Smart, R. S. C. Resolving surface chemical states in XPS analysis of first row transition metals, oxides and hydroxides: Cr, Mn, Fe, Co and Ni. *Appl. Surf. Sci.* **2011**, *257*, 2717–2730.
- (35) Yang, Q.; Wang, X.; Wang, X.; Li, Q.; Li, L.; Yang, W.; Chu, X.; Liu, H.; Men, J.; Peng, Y.; Ma, Y.; Li, J. Surface Reconstruction of a Mullite-Type Catalyst via Selective Dissolution for NO Oxidation. *ACS Catal.* **2021**, *11*, 14507–14520.
- (36) Tang, W.; Wu, X.; Li, D.; Wang, Z.; Liu, G.; Liu, H.; Chen, Y. Oxalate route for promoting activity of manganese oxide catalysts in total VOCs' oxidation: effect of calcination temperature and preparation method. *J. Mater. Chem. A* **2014**, *2*, 2544–2554.
- (37) Sinha, A. K.; Suzuki, K.; Takahara, M.; Azuma, H.; Nonaka, T.; Suzuki, N.; Takahashi, N. Preparation and Characterization of Mesostructured  $\gamma$ -Manganese Oxide and Its Application to VOCs Elimination. *J. Phys. Chem. C* **2008**, *112*, 16028–16035.
- (38) Wu, Y.; Feng, R.; Song, C.; Xing, S.; Gao, Y.; Ma, Z. Effect of reducing agent on the structure and activity of manganese oxide octahedral molecular sieve (OMS-2) in catalytic combustion of o-xylene. *Catal. Today* **2017**, *281*, 500–506.
- (39) Liu, Q.; Duan, X.; Sun, H.; Wang, Y.; Tade, M. O.; Wang, S. Size-Tailored Porous Spheres of Manganese Oxides for Catalytic Oxidation via Peroxymonosulfate Activation. *J. Phys. Chem. C* **2016**, *120*, 16871–16878.
- (40) Li, X.; Ma, J.; Yang, L.; He, G.; Zhang, C.; Zhang, R.; He, H. Oxygen Vacancies Induced by Transition Metal Doping in  $\gamma$ - $\text{MnO}_2$  for Highly Efficient Ozone Decomposition. *Environ. Sci. Technol.* **2018**, *52*, 12685–12696.
- (41) Wu, S.; Liu, H.; Huang, Z.; Xu, H.; Shen, W. O-vacancy-rich porous  $\text{MnO}_2$  nanosheets as highly efficient catalysts for propane catalytic oxidation. *Appl. Catal., B* **2022**, *312*, 121387.
- (42) Feng, B.; Qin, C.; Shi, Y.; Zhang, L. Catalytic Combustion Study of Ethanol Over Manganese Oxides with Different Morphologies. *Energy Fuels* **2022**, *36*, 9221–9229.
- (43) Weng, X.; Sun, P.; Long, Y.; Meng, Q.; Wu, Z. Catalytic Oxidation of Chlorobenzene over  $\text{Mn}_x\text{Ce}_{1-x}\text{O}_2/\text{HZSM-5}$  Catalysts: A Study with Practical Implications. *Environ. Sci. Technol.* **2017**, *51*, 8057–8066.
- (44) Shan, C.; Zhang, Y.; Zhao, Q.; Fu, K.; Zheng, Y.; Han, R.; Liu, C.; Ji, N.; Wang, W.; Liu, Q. Acid Etching-Induced In Situ Growth of  $\lambda$ - $\text{MnO}_2$  over CoMn Spinel for Low-Temperature Volatile Organic Compound Oxidation. *Environ. Sci. Technol.* **2022**, *56*, 10381–10390.
- (45) Hao, X.; Dai, L.; Deng, J.; Liu, Y.; Jing, L.; Wang, J.; Pei, W.; Zhang, X.; Hou, Z.; Dai, H. Nanotubular OMS-2 Supported Single-Atom Platinum Catalysts Highly Active for Benzene Oxidation. *J. Phys. Chem. C* **2021**, *125*, 17696–17708.
- (46) Blumthaler, M.; Ambach, W.; Ellinger, R. Increase in solar UV radiation with altitude. *J. Photochem. Photobiol., B* **1997**, *39*, 130–134.
- (47) Lee, H.; Mayer, H. Solar elevation impact on the heat stress mitigation of pedestrians on tree-lined sidewalks of E-W street canyons – Analysis under Central European heat wave conditions. *Urban For. Urban Greening* **2021**, *58*, 126905.
- (48) Spitschan, M.; Aguirre, G. K.; Brainard, D. H.; Sweeney, A. M. Variation of outdoor illumination as a function of solar elevation and light pollution. *Sci. Rep.* **2016**, *6*, 26756.

## Recommended by ACS

### Effective Toluene Ozonation over $\delta$ - $\text{MnO}_2$ : Oxygen Vacancy-Induced Reactive Oxygen Species

Yuqin Lu, Hong He, *et al.*

JANUARY 23, 2023  
ENVIRONMENTAL SCIENCE & TECHNOLOGY

READ 

### Exceptional Ozone Decomposition over $\delta$ - $\text{MnO}_2/\text{AC}$ under an Entire Humidity Environment

Wenjing Dai, Haibao Huang, *et al.*

MARCH 02, 2023  
ENVIRONMENTAL SCIENCE & TECHNOLOGY

READ 

### In Situ Recovery of Copper: Identifying Mineralogical Controls via Model-Based Analysis of Multistage Column Leach Experiments

Pablo Ortega-Tong, Henning Prommer, *et al.*

MARCH 16, 2023  
ACS ES&T ENGINEERING

READ 

### Beyond Purification: Highly Efficient and Selective Conversion of NO into Ammonia by Coupling Continuous Absorption and Photoreduction under Ambient Conditions

Jieyuan Li, Fan Dong, *et al.*

MARCH 21, 2023  
ENVIRONMENTAL SCIENCE & TECHNOLOGY

READ 

Get More Suggestions >